OPEN ACCESS
IOP Publishing
Journal of Physics D: Applied Physics
J. Phys. D: Appl. Phys. **58** (2025) 045502 (12pp)
https://doi.org/10.1088/1361-6463/ad8ad0

Attenuation of bulk waves using locally resonant soil-coupled metabarriers

Fabio Nistri[1], **Renato Maria Cosentini**[2], **Vinicius F Dal Poggetto**[3,4], **Marco Miniaci**[4], **Paul Charkaluk**[5], **Nicola M Pugno**[3,6], **Antonio S Gliozzi**[1] and **Federico Bosia**[1,*]

[1] Department of Applied Science and Technology, Politecnico di Torino, Corso Duca degli Abruzzi, 10129 Turin, Italy
[2] Departement of Structural, Geotechnical and Building Engineering, Politecnico di Torino, Corso Duca degli Abruzzi, 10129 Turin, Italy
[3] Laboratory for Bioinspired, Bionic, Nano, Meta Materials & Mechanics, Department of Civil, Environmental and Mechanical Engineering, University of Trento, 38123 Trento, Italy
[4] Institut d'Electronique de Microélectronique et de Nanotechnologie, UMR 8520, CNRS, Centrale Lille, University Lille, Junia, Université Polytechnique Hauts-de-France, Lille 59000, France
[5] Phononic Vibes s.r.l., Via Simone Schiaffino 11, 20158 Milano, Italy
[6] School of Engineering and Materials Science, Queen Mary University of London, London, 4NS, United Kingdom

E-mail: federico.bosia@polito.it

Received 28 July 2024, revised 1 October 2024
Accepted for publication 24 October 2024
Published 4 November 2024

Abstract

Low frequency ground-borne vibrations generated by transport infrastructure are one of the most serious causes of disturbance to the general population. One possibility to reduce this problem is to use the wave filtering properties of elastic metamaterials. However, their integration in the soil complicates the prediction of their response, and the influence of soil-structure interaction needs to be correctly evaluated for an efficient design. The aim of this work is to experimentally evaluate the efficiency of metamaterial trench barriers set in soil in attenuating vibrations, using low-frequency local resonance mechanisms. A lab scale model is proposed comprising different resonating structures and a cylindrical encasement is adopted to couple the structure to the soil. The influence of various parameters is evaluated, such as metamaterial structure, geometrical characteristics of the resonator, and constituent materials. Finite Element simulations are used to develop a suitable design, analysing mode shapes and resonance frequencies of structures with and without the surrounding encasement. Experimental modal analysis is then performed on the corresponding fabricated samples, providing both model validation and out-of-soil mechanical characterization. Finally, vibration transmission loss measurements are performed in a setup in which different resonant metamaterial barriers are embedded into the soil sample, allowing the evaluation of barrier performance. Results indicate that the metamaterial structures provide good attenuation of vibrations in selected intervals in the low to high frequency range (1–5 kHz), demonstrating the feasibility of the approach in a scaled sample. Preliminary data regarding the structures providing preferable design characteristics is also obtained. These results can be useful for the design of trench barriers scaled to large dimensions in more realistic applicative settings.

---

[*] Author to whom any correspondence should be addressed.

Supplementary material for this article is available online

Keywords: ground-borne vibrations, vibration mitigation, large-scale vibrations, laboratory-scale tests, finite element method, soil mechanics, locally resonant metamaterials

1. Introduction

Transport-induced ground-borne vibrations are one of the main causes of noise pollution. This is a serious concern for public health, causing high level of annoyance or even adverse effects on sleep [1, 2]. During the past decades, considerable efforts have been devoted to developing efficient and cost-effective solutions for reducing excessive levels of ground-borne vibrations, especially from railway traffic [3–6]. Mitigation measures can be taken either at the source [7], along the propagation path between source and receiver (building) [8–12], or at the receiver [13, 14]. An advantage of interventions on the propagation path is that no modifications to the infrastructure itself are required, while multiple buildings can be protected simultaneously from vibrations. An innovative solution to the problem of ground-borne vibration is the employment of structures enabling passive control of wave propagation using metamaterials (MMs) and phononic crystals (PCs). MMs and PCs are artificially designed materials with superior wave control characteristics, which have been developed in various fields of technology in recent years [15–17]. MMs have been proposed for the control of large-scale vibrations, such as seismic (surface) waves, starting from the theoretical work in [18]. Wang *et al* were the first to present an experimental investigation of the concept, using meter-deep holes in the ground to generate attenuation at 50 Hz for bulk waves [19], and relatively few other experimental studies have followed (e.g. [20]). Since the initial works, many MM designs have been suggested, exploiting both Bragg scattering and local resonance mechanisms to generate high attenuation at low frequencies (below 5 Hz) [21–27], while maintaining technical feasibility. One specific design, termed the ‘resonant metawedge’, theoretically allows to direct surface waves from the surface to the bulk through a mode conversion mechanism from surface to body-waves [28]. Other approaches have been based on the use of single or multiple locally resonant units [29–32]. Analytical approaches have been recently proposed specifically for the modelling of resonating elements in the case of tunnel-radiated waves [33]. Techniques to widen and lower the operational frequency ranges have also been proposed [34–36]. Miniaci *et al* numerically demonstrated the effectiveness of using a hierarchical structure in the design of seismic shields to achieve low-frequency bandgaps (BG) i.e., frequency regions in which wave propagation is inhibited [37]. Thus, MMs have the potential for use in vibration reduction on large scale structures and at low frequencies. Their study and development have become a hot topic in academic research [38–41]. Despite the interest on the topic, experimental studies, both at lab scale [42, 43] and *in situ* [44], have been relatively few, and in some cases, the considered soil was scarcely representative of real world situations (e.g. sandbox experiments). To address this challenge, this study examines the feasibility and effectiveness of trench-like MM structures in reducing soil-coupled bulk waves, focusing on a novel scaled experiment in clay soil. The considered MM unit cells (UC), are based on designs enabling large BG deriving from previous work by the authors [21, 22], including hierarchical designs [45], which were found in some cases to enable widening of the BG and their shifting to lower frequencies. Investigations are conducted on a lab-scale model, requiring a rescaling of sample dimensions and frequency ranges. While full-scale buried trench barriers in literature are typically around 10 m, with operating frequencies of tens of Hz [46, 47], the samples in this work are approximately 10 cm in size and 3 mm thick, shifting the frequency range from 10–50 Hz to 0.1–5 kHz. Due to lab constraints, the problem is simplified to normal wave incidence on the barrier. Only propagation through soil is considered, excluding surface modes. Although the experimental conditions differ from real-world scenarios, this setup offers valuable insights into inertial soil-structure interaction effects (i.e. how the soil alters resonance properties [48]), validates numerical models, and assesses the solution’s effectiveness in reducing soil-coupled vibrations.

The outline of the paper is as follows. Section 2 introduces the simplifications and the scaling considered to manufacture a lab scale setup. The design and fabrication of the samples and experimental setup is presented in section 3. The results of the numerical simulations are shown in section 4. In section 5 experimental results are compared to numerical simulations and further discussed. Section 6 is dedicated to soil fabrication and characterization. Experimental results of the designed trench barrier in contact with the soil are presented and discussed in section 7. The scaling of results to large dimensions and realistic structures is discussed in section 8.

2. Sample design and manufacturing

MMs are artificial structures whose properties can be derived from those of its representative UC, which are periodically arranged to form a ‘crystal’ [49]. Here, the starting idea of the UC design was to exploit coupled ‘resonance-Bragg’ BG [50–52] and to employ this mechanism for the attenuation of bulk waves in soil. Two structures are selected, based on previous studies in which favourable BG characteristics were found [21] (see figure 1). The first, named central resonator (CR), displays a low frequency BG due to the resonance-Bragg mechanism, similarly to the second geometry named four-leaf clover (FLC). To illustrate in general their vibrational characteristics, in view of their potential use in trench barriers where they can be arranged periodically in an array, we first calculate their dispersion diagrams using finite element (FE) simulations for a

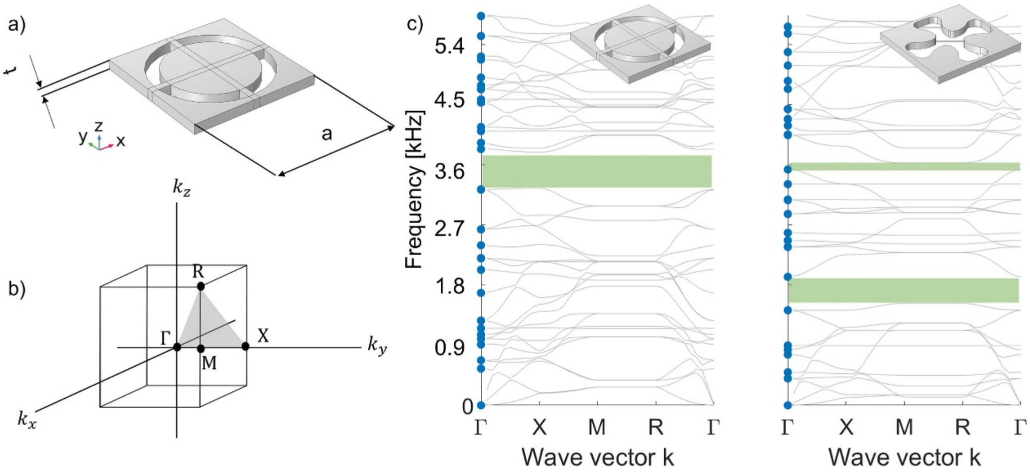

Figure 1. (a) Schematic of the characteristic sizes of a typical UC and (b) the first Brillouin zone with the irreducible part (light grey triangle of vertices Γ-X-M-R-Γ) for a cubic UC. (c) Dispersion diagrams for CR and FLC structures: points in blue correspond to the eigenmodes of the UC with free–free boundaries.

3D cubic irreducible Brillouin zone (IBZ, figure 1(b)) applying the Bloch–Floquet boundary conditions only in the xy plane, due to the geometry of the problem. No periodicity is assumed in the normal direction (perpendicular to the barrier).

The dispersion diagrams shown in figure 1 are calculated for a lattice size of $a = 126$ mm, and $a/t = 3$ for CR and FLC geometries. The materials properties are Young's modulus $E = 1$ GPa, density $\rho = 1.1 \cdot 10^3$ kg m^{-3}, and Poisson's ratio $\nu = 0.4$.

The two geometries are similar, in that both correspond to a CR connected by four lateral springs to an external frame (see also figure 2). As a result, the modal behaviour is similar, apart from a larger number of vibration modes in the FLC geometry due to the non-circular geometry of the CR. In addition, it is possible to compute a bandgap coverage (BGC) [53, 54] as $\mathrm{BCG} = \frac{\mathrm{SBG}}{F_{\max} - \mathrm{SBF}} \cdot 100$, where SBG is the sum of the BG bandwidths and $F_{\max}$ is the highest frequency of the calculated dispersion relation. The values of the BGC for the CR and FLC are 9.9% and 8.1% respectively. As already investigated in [21], the lateral size to thickness ratio is one of the main parameters determining the ranges in which this type of BG occurs. Together with the dimensions of the systems, the mechanical properties of the medium influence the dispersion relation of the MM, as investigated carrying out a parametric study on the FE model of the samples (see figure SM1 in the supplementary material).

For the remainder of the work, the geometries of these UCs are implemented in a lab-scale cylindrical geometry with a diameter of $D = 126$ mm (figures 2(a) and (b)), due to experimental and fabrication constraints, while the other dimensions are chosen so as to maintain the proportions with the original UCs [21]. This implies a scaling of the BG frequencies from tens of Hz (required in applications) to the kHz range (see discussion in section 7). Also, the use of a cylindrical geometry instead of the square-section UC analysed in figure 1 leads to some variation in the modal spectrum of the structure. However, as discussed in the supplementary material, differences are negligible for the lowest eigenfrequencies, and the BGs in figure 1 can be considered indicative of the frequency ranges where vibration transmission is also inhibited in the cylindrical geometry. We also notice that, for both cases, the highlighted BGs are persistent with respect to all wave vectors (i.e. full BGs), also indicating that partial BGs are present for waves propagating in the thickness direction (i.e. outside of the ΓX and XM direction).

A first set of locally resonant plates is designed with a UC size equal to the diameter of the plate to target low resonance frequency eigenmodes, while two additional designs are conceived to explore the possibility of scaling local resonance of the considered structures and extend their working frequency (figures 2(d) and (c), since previous studies have shown that implementing hierarchical UC design can in some cases widen BG and shift them to lower frequencies [45]. To couple the structures to the soil vibration while allowing their free vibration, an encasement is designed, as shown in figure 2(e). The bulk waves in the soil impinge perpendicularly on the barrier and propagate along the axis of the cylinder (figure 2(f)).

The two sets of samples were fabricated with different thicknesses, due to the manufacturing constraints, of 10 and 3 mm for the polymeric (PLA) and metallic samples, respectively. The set of PLA samples was fabricated in the laboratories using 3D printing with fused filament fabrication on a Dremel DigiLab 3D45 printer. The process parameters included a 100% filling factor and a layer thickness of 0.34 mm. A second set of samples, made of steel, was fabricated using a laser cutting technique.

3. Numerical modelling of locally resonant plates

A FEM study of the eigenmodes of the fabricated samples with clamped boundary conditions on the external UC boundary was first performed to determine the resonance frequencies of the resonating structures. To explore the behaviour of the structures for the selected range of frequencies, a forcing term is added to the elastodynamic problem through the

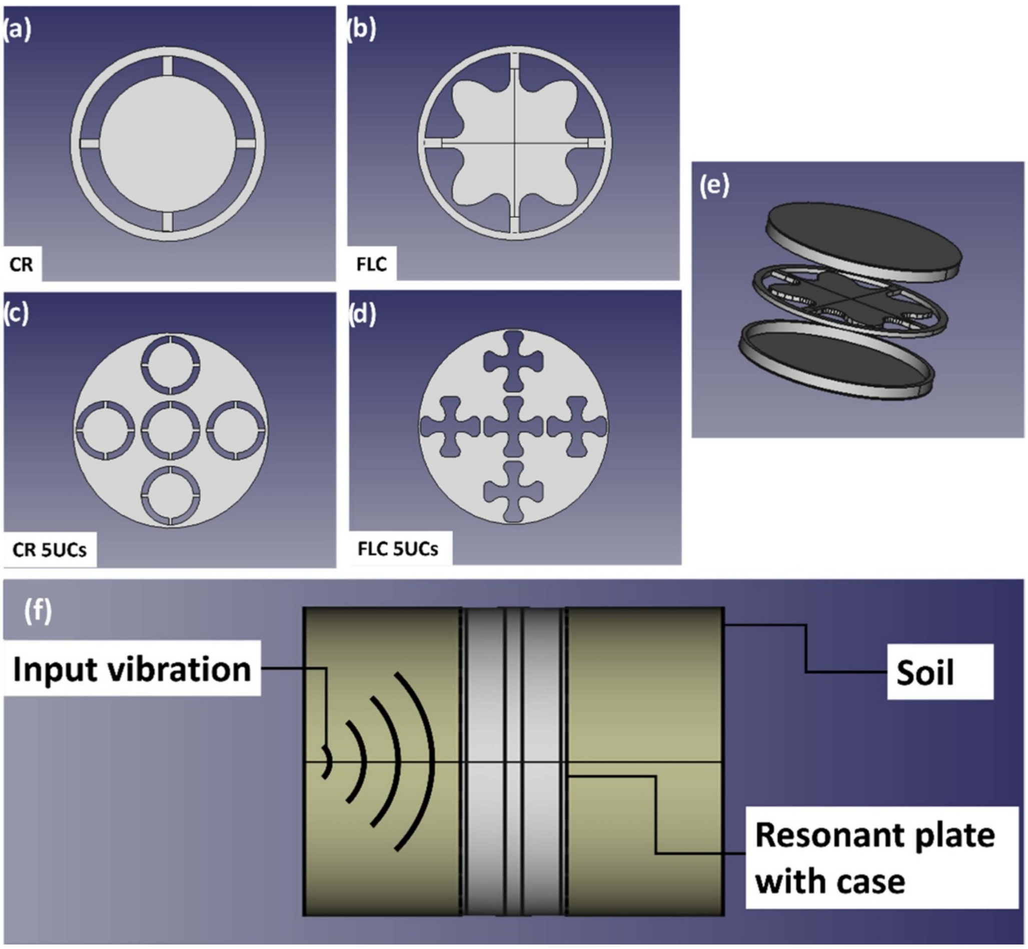

Figure 2. Unit cell design and experimental configuration: (a) adapted UCs design for CR and (b) a modified version of the FLC resulting from a translation of the UC by a half lattice parameter. (c) CR and (d) FLC with five UCs arranged in a cross-like array to fill the diameter with the largest possible number of UCs of lattice parameter of $1/3$ of the diameter. (e) Exploded view of the assembly formed by the case parts and the inclusion. (f) Schematic of the experimental design setup in which the resonant plate and encasing are embedded in soil portions.

application of a normal unit force $F = Ae^{i\omega t}$, with $A = 1$ N, on a specified area at the centre of the plate, mimicking the location of the piezoelectric actuator in the experimental setup. The response of the structure is measured as the surface average of the normal velocity amplitude on the opposite surface to where the force is applied. This type of study allows to determine the expected spectrum of the response of the resonating structure to a wide band excitation (frequency sweep or burst), highlighting the location of the maxima (resonating frequencies). The frequency response function (FRF) of the resonant plate connected to the case can be correlated with the resonance frequencies of the corresponding isolated UC plate clamped at its edges, which mimics the effect of a rigid encasement. As a consequence, the frequencies in which an effective excitation of the plate is achieved (i.e. its resonance frequencies) are linked with the transmission of energy along the encasement, resulting in significant displacements of the internal UC, and generating overall plate-case system anti-resonances (minima in the computed FRF). Results are shown in figure 3 for the PLA CR structure, chosen as an example. While there is matching for the first eigenmode (indicated with (i)), other plate resonances do not exactly coincide with the anti-resonances of the plate-case system. This coupling can be explained due to the more efficient excitation of the corresponding vibration mode of the resonator, which occurs for modes that involve transverse displacement of the central mass of the structure, while other types of resonances (bending or torsional) present less significant out-of-plane displacements in the resonator central mass. It is also interesting to notice that a reasonable dip in the FRF is observed around the frequency of 3.6 kHz, which corresponds to the centre of the BG highlighted in figure 1(c) (left panel). This system is subsequently coupled to the soil in experiments.

4. Experimental characterization of meta-resonator samples

To validate the numerical model, the resonant structures are tested performing an experimental modal analysis with the setup shown in figure 4. The plates are excited on the bottom

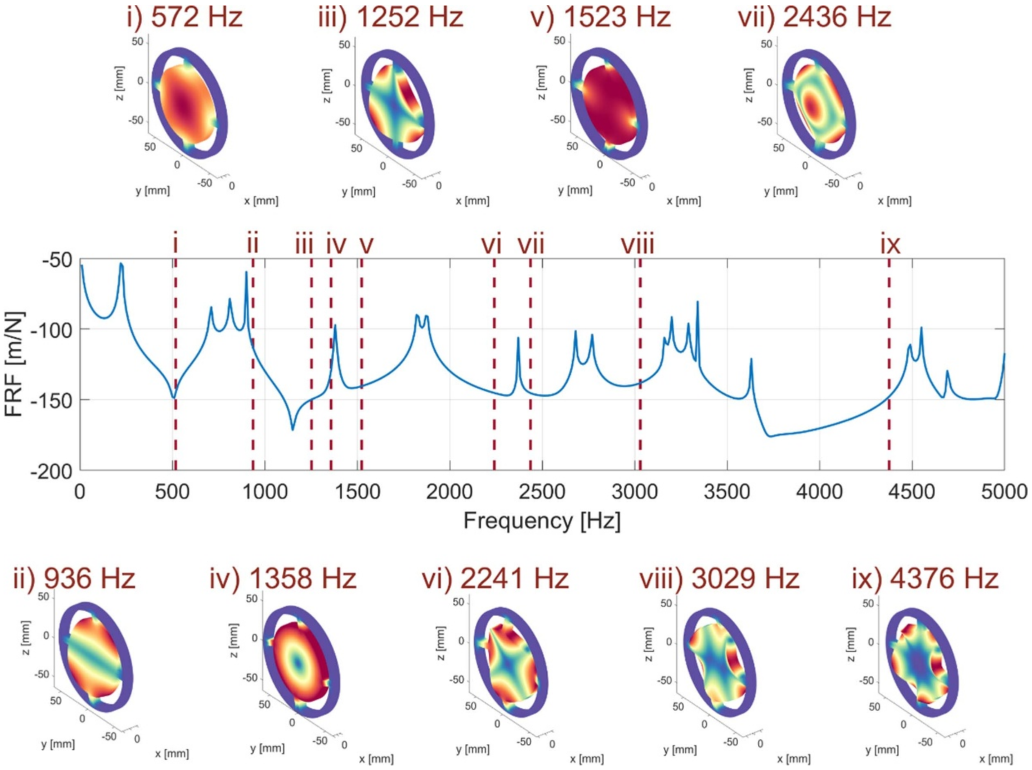

Figure 3. Frequency response function (FRF) of the CR plate in the cylindrical case, compared to the simple CR (clamped) plate modal shapes and frequencies, indicated with letters from (i) to (ix).

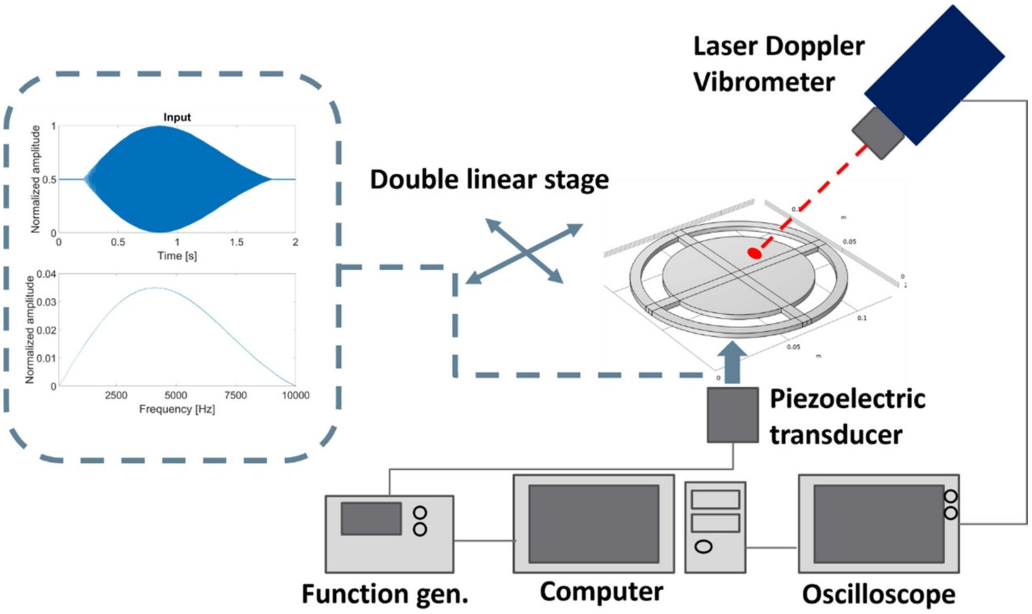

Figure 4. Schematic of the setup and inset with the input function used in time and frequency domain.

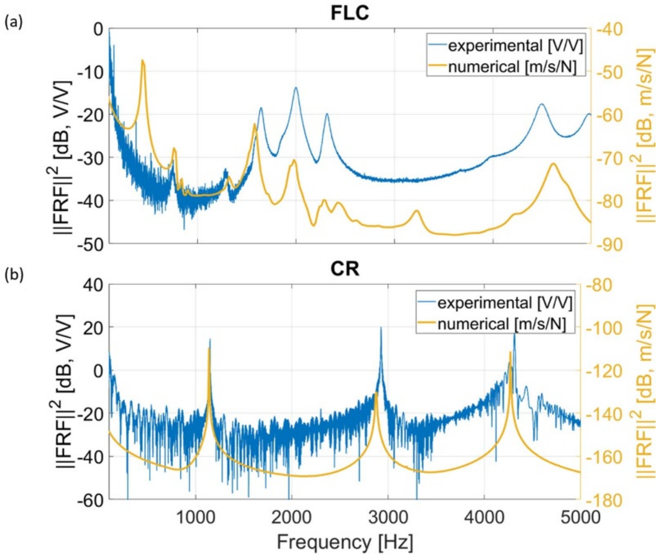

Figure 5. Comparison between the experimentally measured and numerically calculated FRFs averaged over the whole top surface of the sample for (a) PLA FLC and (b) steel CR.

surface using a piezoelectric transducer placed in the centre of the plate with a linear sweep signal (duration $\Delta t = 2$ s), over a frequency range from 0.1 to 5 kHz. The acquisition is performed scanning the top surface with a Laser Doppler Vibrometer (LDV).

The measured input and output signals are analysed calculating the average of the square FRF magnitude, i.e. analysing the average energy of the signal for a unit energy input:

$$\|\mathrm{FRF}(f)\|^2 = \frac{\frac{1}{N}\sum_{i=1}^{N} Y_i(f)^2}{\|X(f)\|^2}, \tag{1}$$

where $Y_i(f)$ is the Fourier transform of the output signal in the ith point, N the total number of scanned points, and $X(f)$ is the Fourier transform of the input signal. This quantity is indicative of the energy of the measured response. The average value of the function over all scanned points is taken as reference. Although some modes in which nodal points occur at the centre of the plate are not excited efficiently due to the location of the source, the FE model can be calibrated with sufficient accuracy using non-axisymmetric modes. The amplitude of the FRF function for the numerical simulation is computed using the force (N) as input and velocity (m/s) as output, while for the experimental one the input and output are the signals in volts (V) from the piezo-patch and LDV, respectively. Fair agreement is found for PLA samples, as shown in figure 5(a), in which the resonance peaks in the frequency range between 1.5 and 2.5 kHz are correctly predicted, together with some minor peaks at lower and higher frequencies. The imperfect match can be due to the numerical reproduction of boundary conditions, and possibly to a frequency mismatch due to the viscoelastic behaviour of the material arising in experiments [55]. For the steel samples, the numerical results of modal shapes and respective resonances are compared to an experimental measurement of the respective sample performed scanning the response in just one point. Here, excellent agreement is found between the experimental and numerical FRF functions at all resonance frequencies (figure 5(b)).

In addition, the configuration of the resonant plate within the case is compared with the experimental FRF, as shown in figure 6. Here, we observe a good overall match between the experimental and numerical results due to the introduction of damping for the PLA parts. However, viscoelastic effects are neglected, and this results in a mismatch for frequencies above 2 kHz. For this reason, higher frequencies are not reported. As shown in greater detail in the supplementary material, we observe that ‘hierarchical’ configurations (5 UCs) do not display significant advantages in the simulated/measured spectra, in terms of lower/wider resonances, compared to the non-hierarchical ones. This is due to insufficient degrees of freedom in modifying the geometry of the samples to enable sufficient reduction in the effective flexural stiffness while maintaining similar inertial effects in the resonating elements [45] Therefore, only results relative to non-hierarchical geometries are discussed in the remainder of the paper.

With the same acquisition method described in the previous paragraph, in many cases, it is possible to prove the presence of structural attenuation in the transmission spectra of the resonator-case with case in correspondence with (w/) the resonating frequencies of the structures without (w/o) the case. This is noticeable because the maxima of the spectra for the specimens without case coincides with the minima of those for the specimens with case. This is shown for example in figure 7, for the FLC and CR 5UCs geometries in PLA and steel, respectively. It is also important to notice that there is a substantial decrease in the FRF in the FLC case due to the losses associated with the PLA material. In the case of the CR geometry, such significant losses are not observed when using a steel casing. The complete results for all UC configurations are shown in the supplementary materials (figures SM1 and SM2).

5. Characterization of the soil sample

Experimental tests are performed on meta-resonators embedded in a soil sample to evaluate the performance of the different designed systems when including inertial soil-structure interaction effects. The soil sample is a reconstituted White China Clay Kaolinite (78.5% of clay, 21.5% of silt). The specimen is prepared in a consolidometer (diameter $D = 15.5$ cm and total height $H = 20.0$ cm) under a vertical effective pressure of 100 kPa. At the end of consolidation process, the specimen is extruded and sampled to obtain two homogenous samples with a diameter of 13 cm and a height of 4 cm. The main characteristics of both samples are reported in table 1.

One of the two soil samples was transferred in a non-standard oedometer (shown in figure 8) for a preliminary geophysical characterization in terms of compression and shear wave velocities. The apparatus was specifically designed to perform 3D electric resistivity tomography and to measure the velocity of compressional (P) and shear (S) waves together

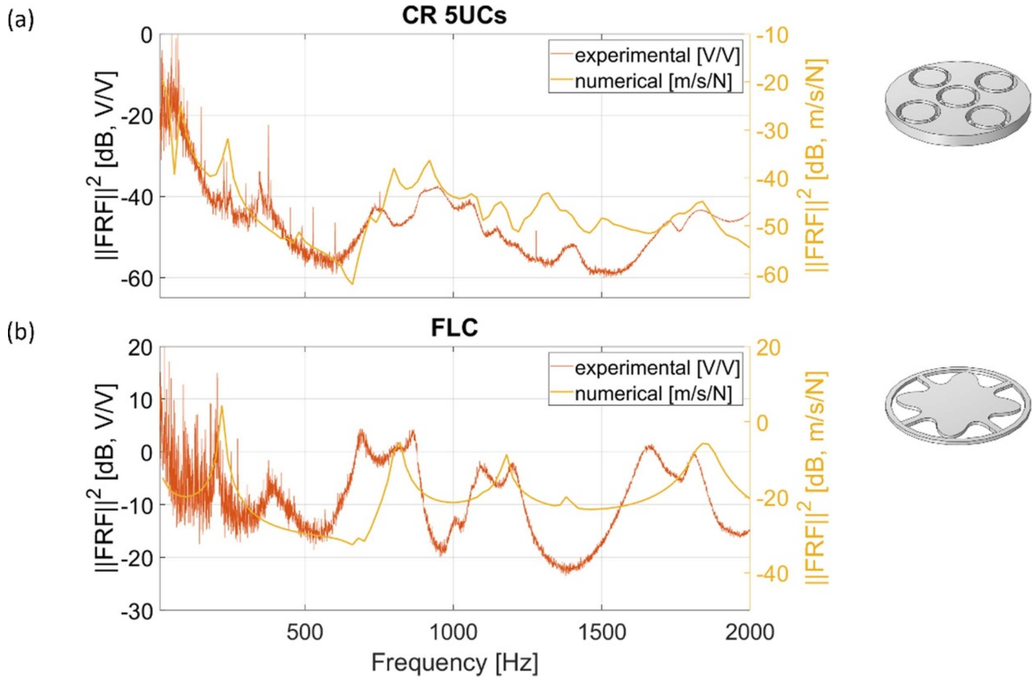

Figure 6. Experimentally measured and numerically calculated FRFs for (a) the PLA CR 5UCs and (b) steel FLC.

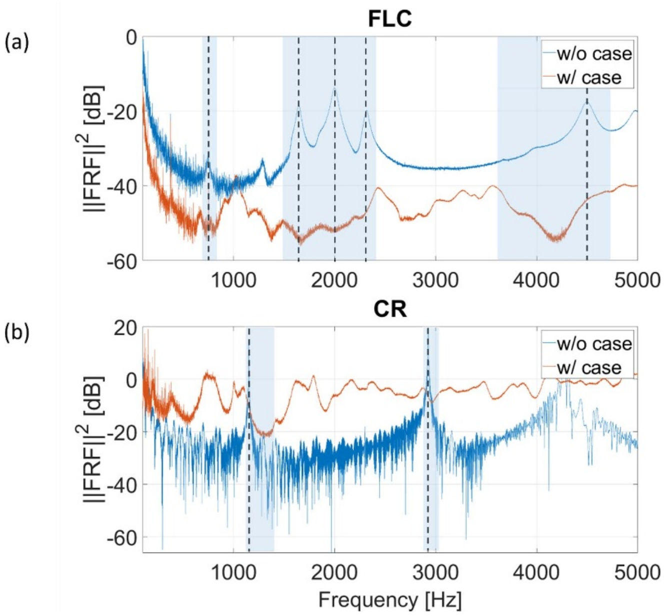

Figure 7. Comparison between the measured FRFs, without (w/o) and with (w/) the case, for (a) the polymeric (PLA) FLC and (b) steel CR geometries. The correspondence between the resonance frequencies of the structure (w/o) and the transmission loss of the encased structure (w/) is highlighted by the black vertical dashed lines.

Table 1. Main physical characteristics of soil sample.

Water content, w (%)	48.5	Liquid limit, w_L (%)	53.85
Density of soil, ρ (kg m^{-3})	1645	Plasticity index, PI (%)	22.8
Void ratio, e_0 $(-)$	1.378	Specific gravity, G_S $(-)$	2.62

with conventional external measurements [56]. In this test, the device is only used to confine the sample laterally and to measure wave velocities. In this respect, the wave velocities are measured on the base of a time of flight (ToF) approach, as shown in figure 8. For both P- and S-wave generation, the material is excited using a periodic sinusoidal burst (figure 8(b)). Due to several disturbances affecting the signal recorded at the receiver (e.g. electromagnetic coupling and crosstalk between the piezoelectric transducer, reflection, and refraction phenomena), the wave velocities are computed by selecting both the first arrival and the peak value corresponding to the third reflection, for the P-wave (figure 8(c)), or the fifth one, for the S-wave (figure 8(d)). For the S-wave, the first arrival does not correspond to the actual start of the signal. This phenomenon is identified as a directivity issue due to the bender element transducer used and described in [57]. A comparison of different approaches for evaluating wave velocities is therefore necessary. Tables 2 and 3 report the P-wave (c_L) and S-wave (c_T) velocities, respectively, computed using the two different ToF estimates, and an evaluation of the uncertainty in the results applying the two different approaches. While for the P-wave the uncertainty is small, and thus the two approaches to estimate the velocity of waves are equivalent, in the S-wave case there is a larger uncertainty due to a signal bias corresponding to the arrival of the reflected P-wave, which makes the first arrival of the other component difficult to read. Therefore, we use the value of the S-wave velocity (c_T) determined with the fourth reflection and the P-wave velocity (c_L) evaluated with reference to the first arrival for the calculations of mechanical parameters of soil. The obtained mechanical properties of soil are $\mu = 134$ MPa and $\lambda = 252$ MPa, corresponding to a Young's modulus $E = 356$ MPa and $\nu = 0.33$.

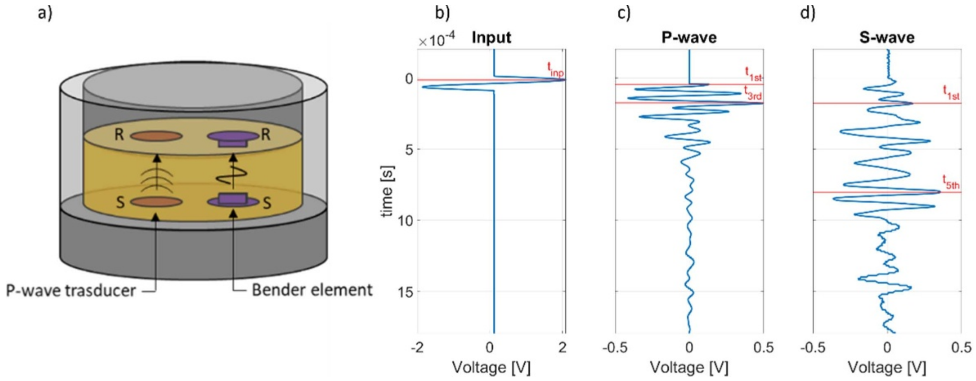

Figure 8. Soil characterization: (a) Experimental set-up for the geophysical characterization of soil (R: receiver—S: Source). (b) input burst excitation of soil where t_{inp} is the reference time instants to determine the ToFs for both mentioned cases. (c) output response for the P-wave signal where t_{1st} and t_{3rd} are the assumed first arrival and third reflection time, respectively. (d) output signal related to the S-wave were t_{1st} and t_{5th} correspond to the first arrival and second reflection respectively.

Table 2. ToF data for the S-wave characterization.

First arrival	Third reflection
$\Delta t = 550 \times 10^{-5}$ s	$\Delta t = 160 \times 10^{-4}$s
$L = 300 \times 10^{-2}$ m	$L = 900 \times 10^{-2}$ m
$c_L = 545$ m s^{-1}	$c_L = 563$ m s^{-1}
$\%\epsilon = 320$ %	

Table 3. ToF data for the P-wave characterization.

First arrival	Fifth reflection
$\Delta t = 172 \times 10^{-4}$ s	$\Delta t = 779 \times 10^{-4}$ s
$L = 340 \times 10^{-2}$ m	$L = 102 \times 10^{-1}$ m
$c_T = 206$ m s^{-1}	$c_T = 285$ m s^{-1}
$\%\epsilon = 2772$ %	

6. Experimental test of meta-resonator embedded in a soil sample

Tests for the evaluation of the performance of meta-resonators in contact with the soil are performed by adopting a 'sandwich' experimental setup, in which the resonating plate/case is placed between the two soil samples, prepared as described above. This simplified setup allows to simplify measurements and ensure a clear interpretation of results. The entire system is encased in the modified oedometer cell to provide lateral confinement. At the bottom of the soil, a piezo buzzer element is placed as an excitation source. The adopted input signal is a sweep (duration $\Delta t = 2$ s) with a frequency spectrum ranging from 0.1 to 5 kHz. Frequencies above 5 kHz are not considered due to the high damping regime observed in the soil samples above this value. The output is recorded using a laser Doppler vibrometer on the top surface of the soil. The data is then analysed calculating the FRF function of the input and output signals. The setup is illustrated in figure 9.

Results for PLA and steel samples are illustrated in figure 10, in which the FRF of the resonant plate/case systems is reported for in and out of soil tests. The complete results for all UC configurations is shown in the supplementary material (figures SM3 and SM4). Attenuation regions emerge in different specific frequency ranges for all MM designs. Although the attenuation of bulk waves by the metabarriers should be validated by relative comparisons with experiments in soil without the barriers, data from [5] indicates that the frequency response for the type of considered soil is relatively flat in the frequency range of interest. This suggests that any features appearing in the FRF spectrum can be attributed to the metabarrier itself, rather than to the soil.

To verify if these attenuation ranges coincide with the resonances of the UC structures, the FRF comparison plot between the resonant plate and resonant plate/case shown in the previous section was used. In particular, for the CR geometry there is a relatively good match between the central attenuation range in the out- and in-soil configuration, whereas the other two frequency attenuation ranges do not appear in the in-soil results (figure 10(a)). For the FLC geometry, there is a partial coincidence between two regions of attenuation in- and out of-soil, as shown in figure 10(b). In the two cases, the attenuation occurs at a wavelengths of approximately $\lambda = 27$ mm for P-waves and $\lambda = 13$ mm for S-waves.

In terms of attenuation, these results are comparable to others reported in the literature. In [6], the assessment of wave barriers for ground borne application was conducted in a 'sandbox' test for a combined solid and empty trench, showing a 40% decrease in acceleration amplitude. Instead, in [11] a locally resonant MM array tested in a 3 × 3 × 0.8 m sandbox showed a decade of acceleration decrease in a frequency range spanning from 160 to 400 Hz. An in-field test result was studied in [31], where a 40 m long locally resonant meta barrier provided an insertion loss of 10 dB at the resonance frequency of 32 Hz up to a distance of 32 m far from the trench. The metabarrier proposed in this work should provide similar performances at the designed working frequencies, although we are considering a simplified setup in which surface waves, resonant scattering or geometric scattering effects, wave conversion, etc. do not play a role.

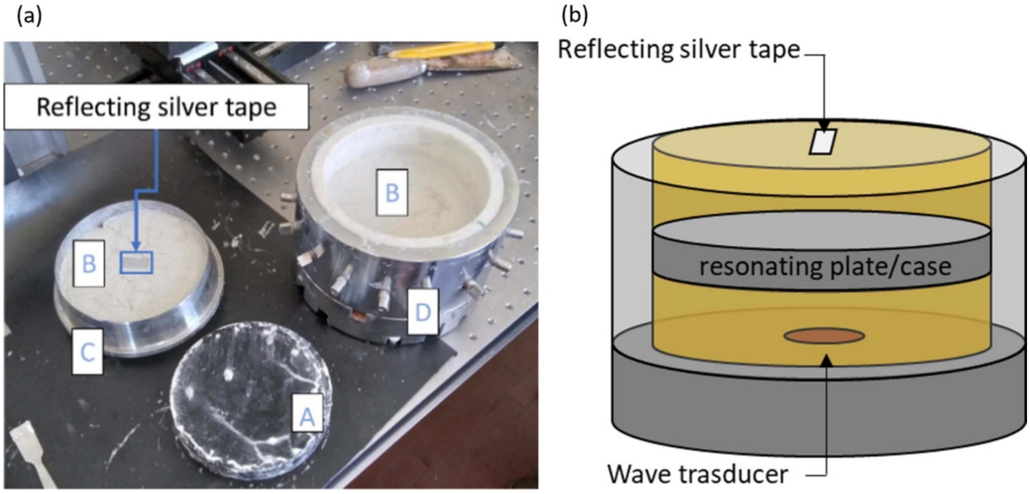

Figure 9. Experimental setup: (a) disassembled oedometer cell for in-soil tests with (A) resonant plate/case system and (B) soil samples. (C) Steel sampling ring here used to ensure plane strain boundary condition on lateral sides of the top soil portion. (D) Modified oedometer cell and assembled oedometer cell for in-soil tests. (b) Schematic of the experimental setup.

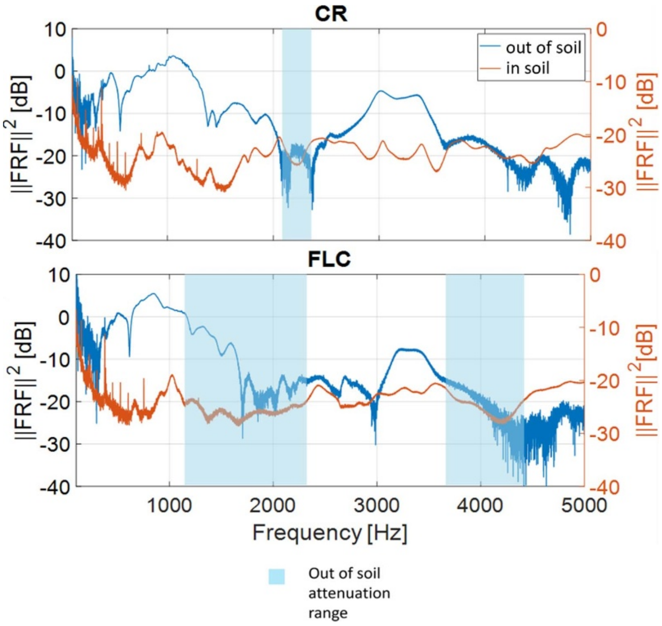

Figure 10. FRF functions for the output signal of in soil (red line) and out of soil (blue line) test for (a) the PLA FLC and (b) CR samples.

7. Scaling

A comparative analysis of the dependence of sample dimensions on the natural frequencies of the system is finally performed to assess how the considered structures should be scaled to address the low-frequency ground-borne vibration problems cited in the Introduction. Due to the complex mechanisms involved in the inertial soil-structure interaction, we refer to the correlation between FRF and the internal resonator behaviour (figure 3), considering the transverse vibration of the internal UC as the fundamental mechanism responsible for the attenuation of impinging waves on the system. Additionally, the casing is considered as a rigid substrate compared to the stiffness of its attachment to the internal UC. As a result, we approximate the internal UC using lumped parameters to represent its effective stiffness and mass. Although simplified, this model still allows to compute the first transverse resonance frequency of our system. As an example, the PLA CR sample is chosen (figure 11(a), top row), which can be approximately modelled as a spring-mass structure (figure 11(a), bottom row), with the four connecting beams playing the role of the springs (orange in figure 11(a)) and the internal cylinder (light blue in figure 11(a)) that of the mass.

The first resonance frequency can then be calculated as $\omega_n = \sqrt{\frac{4k}{m}}$, where k is the total stiffness of each beam and m is the mass of the suspended central disk. The stiffness of each beam is given by $\frac{1}{k} = \frac{1}{k_b} + \frac{1}{k_s}$, where $k_b = \frac{3EI}{L^3}$ is the

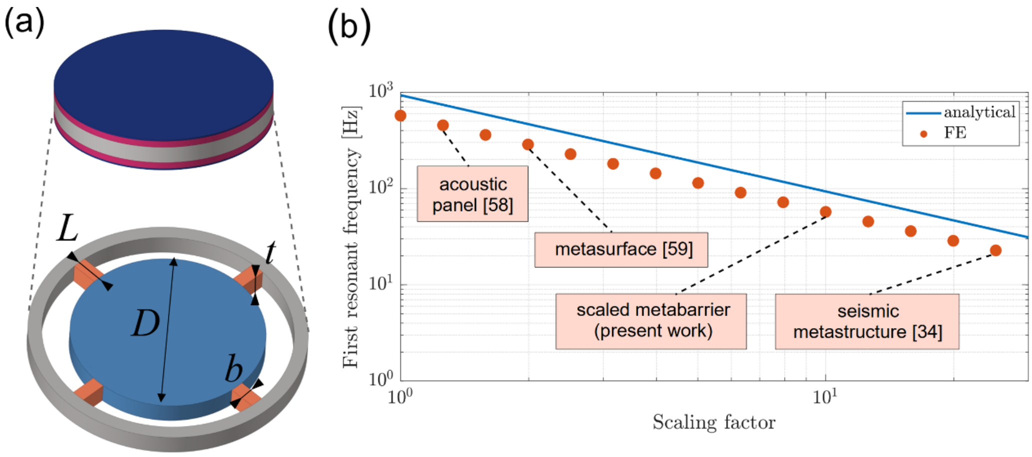

Figure 11. Investigation of the effects of scaling parameters on the first resonant frequency of the resonator. (a) Considered polymer CR sample, with internal diameter (D), width (b) and length (L) of the supporting structures, and thickness t. (b) Effect of the scaling factor (s). The first resonant frequency, calculated analytically and numerically, is associated with the longitudinal (out-of-plane) vibration.

bending stiffness, with E the beam material's Young modulus, I the moment of inertia of its cross-section, and L its length; $k_s = t_s \frac{Gbt}{L}$ is the beam's shear stiffness, with $t_s$the shear factor, $G = \frac{E}{2(1+\nu)}$ the elastic shear modulus for the material and Poisson's coefficient ν; b and t are, respectively, the width and height (thickness) of a beam with rectangular cross-section, in which case, $I = \frac{bt^3}{12}$ and $t_s = \frac{6}{5}$. The mass of the disk is given by $m = \rho \frac{\pi D^2}{4} t$, where ρ is the material specific mass density and D the disk diameter, having a thickness equal to that of the beams. Substituting these quantities gives the approximate expression $\omega_n = \sqrt{\frac{4Ebt^2}{\pi \rho D^2 L^3} \frac{1}{1+\frac{1+\nu}{2t_s}\left(\frac{t}{L}\right)^2}}$. The corresponding lowest resonant frequencies are compared with FE simulations considering the scaling factor s equally applied to all the dimensions of the resonator. Figure 11(b) shows the corresponding frequency values of the first vibration mode obtained using FE models (red dots) considering clamped conditions for the outer edges (i.e. including the grey part in figure 11(a)), while the analytical expression for the approximated resonant frequency (blue curve) confirms the locally resonant behaviour of all computed frequencies. For the initial size ($s = 1$), the resonator of thickness $t = 10$ mm and external diameter of 126 mm has a first resonant frequency at 933 Hz. This frequency is scaled down to 466 Hz for an external diameter 251 mm ($s = 2$), 187 Hz for 631 mm ($s = 5$), and 93 Hz for 1.26 m ($s = 10$). The overestimation of the analytical curve with respect to the FE results (figure 11(b)) is probably due to the lower stiffness associated with the casing, when compared to infinitely rigid endings for the beams considered in the analytical solution. The trend of both curves, however, is clearly correlated. This scaling relation is consistent with laboratory model (1 g) scaling laws, and may also be useful to evaluate the considered design for applications in other fields, such as the design of locally resonant structured panels [58], subwavelength metasurfaces [26], or seismic metastructures [34], whose typical working frequencies are also shown in figure 11(b).

8. Conclusions

In summary, this work has discussed the possibility of using soil-coupled MM barriers for the attenuation of bulk waves. The effectiveness of using a relatively thin obstacle perpendicular to the direction of vibration propagation at low frequencies (large wavelengths) has been assessed. To aid this evaluation, we have performed a numerical and experimental study of a lab-scaled model on the effect of resonant barriers on the propagation of bulk elastic waves in soil. The scaled model comprised various resonating structures originating from two main MM designs, based on local coupling of resonance and Bragg BGs. A cylindrical encasement was adopted to couple the structures to the soil, while allowing the resonators to freely vibrate. The work analysed the influence of various parameters on the chosen solution: resonating structures were fabricated in PLA and steel materials with (different thicknesses) and two different UCs were tested, with two different lattice parameters and filling fractions. This allowed to consider periodically repeated UC for two of the designs.

The chosen overall cylindrical geometry allowed to simplify the geometrical aspects of the problem of ground-borne vibrations, eliminating surface effects related to the half space geometry, and thus the presence of surface (Rayleigh) waves and mode conversion effects. This allowed to evaluate the performance of the barrier configuration in a simplified manner, facilitating the correlation between the MM structure, vibration properties, and the overall barrier transmission characteristics.

In general, the numerical-experimental investigation allowed to demonstrate the presence of structural attenuation in the transmission spectra in correspondence with some of the resonating modes of the MM structures, in relatively low frequency ranges. Some influence of MM design emerged in the effective frequency attenuation regions, especially where local resonance effects were more pronounced. Thicker PLA barriers also seem to be more promising, due to the enhanced inertial effect, coupled with viscoelastic damping.

Further work is required to evaluate the efficiency of the solution compared to other designs in more realistic setups, e.g. in a half-space configuration, considering surface wave propagation, scattering and wave conversion effects. However, from these preliminary results, the proposed barrier concept for soil vibration mitigation appears to be feasible and would allow frequency tunability in low-frequency attenuation. From an applicative point of view, it could be particularly attractive, since the barriers could be fully buried in the ground alongside the infrastructure generating the vibrations, at a distance of a few metres, thus providing a non-invasive solution. Progress in this field could lead to significant benefits in terms of sustainability of transport infrastructure, particularly in densely populated urbanized areas.

Data availability statement

The data cannot be made publicly available upon publication because the cost of preparing, depositing and hosting the data would be prohibitive within the terms of this research project. The data that support the findings of this study are available upon reasonable request from the authors.

Acknowledgment

FN, VFDP, MM, PC, NMP, ASG and FB acknowledge the European Commission under the FET Open “Boheme” Grant No. 863179 and FET Launchpad “BioMetaRail” Grant No. 101034634.

Data access statement

Data from this paper will be provided by the authors upon reasonable request

Conflict of interest

All authors declare that they have no conflicts of interest.

ORCID iDs

Fabio Nistri https://orcid.org/0009-0006-4629-5686
Renato Maria Cosentini https://orcid.org/0000-0002-7080-2186
Vinicius F Dal Poggetto https://orcid.org/0000-0003-0862-6270
Marco Miniaci https://orcid.org/0000-0002-6830-3548
Paul Charkaluk https://orcid.org/0009-0001-5820-4861
Nicola M Pugno https://orcid.org/0000-0003-2136-2396
Antonio S Gliozzi https://orcid.org/0000-0003-1084-0444
Federico Bosia https://orcid.org/0000-0002-2886-4519

References

[1] Maclachlan L, Ögren M, van Kempen E, Hussain-Alkhateeb L and Persson Waye K 2018 Annoyance in response to vibrations from railways *Int. J. Environ. Res. Public Health* **15** 1887

[2] Waddington D, Woodcock J, Smith M G, Janssen S and Waye K P 2015 CargoVibes: human response to vibration due to freight rail traffic *Int. J. Rail Trans.* **3** 233–48

[3] Costa P A, Calçada R and Cardoso A S 2012 Ballast mats for the reduction of railway traffic vibrations.Numerical study *Soil Dyn. Earthq. Eng.* **42** 137–50

[4] Loy H 2012 Mitigating vibration using under-sleeper pads *Railw. Gazette Int.* **168** 40–43

[5] Lombaert G, Degrande G, Vanhauwere B, Vandeborght B and François S 2006 The control of ground-borne vibrations from railway traffic by means of continuous floating slabs *J. Sound Vib.* **297** 946–61

[6] Cao X, Zhou F, Liu J and Ma Q 2024 Experimental study and numerical analysis for vibration isolation performance on open trench and wave impeding block combined vibration isolation barrier *Soil Dyn. Earthq. Eng.* **177** 108418

[7] Zeng Z, Qahtan A A S, Hu G, Xu R and Shuaibu A A 2023 Comparative experimental investigation of the vibration mitigation characteristics of ballasted track using the rubber composite sleeper and concrete sleeper under various interaction forces *Eng. Struct.* **275** 115243

[8] François S, Schevenels M, Thyssen B, Borgions J and Degrande G 2012 Design and efficiency of a composite vibration isolating screen in soil *Soil Dyn. Earthq. Eng.* **39** 113–27

[9] Karlström A and Boström A 2007 Efficiency of trenches along railways for trains moving at sub-or supersonic speeds *Soil Dyn. Earthq. Eng.* **27** 625–41

[10] Hung H H, Yang Y B and Chang D W 2004 Wave barriers for reduction of train-induced vibrations in soils *J. Geotech. Geoenviron. Eng.* **130** 1283–91

[11] Li Z, Ma M, Liu K and Jiang B 2023 Performance of rubber-concrete composite periodic barriers applied in attenuating ground vibrations induced by metro trains *Eng. Struct.* **285** 116027

[12] Ni Y and Shi Z 2023 Dynamic analysis of an elastic half-plane soil medium with periodic wave barriers under a moving load *Eng. Struct.* **278** 115544

[13] Newland D E and Hunt H E M 1991 Isolation of buildings from ground vibration: a review of recent progress *Proc. Inst. Mech. Eng.* C **205** 39–52

[14] Talbot J P and Hunt H E M 2003 A generic model for evaluating the performance of base-isolated buildings *J. Low Freq. Noise Vib. Act. Control* **22** 149–60

[15] Lu M-H, Feng L and Chen Y-F 2009 Phononic crystals and acoustic metamaterials *Mater. Today* **12** 34–42

[16] Krushynska A O, Torrent D, Aragón A M, Ardito R, Bilal O R, Bonello B, Bosia F, Chen Y, Christensen J and Colombi A 2023 Emerging topics in nanophononics and elastic, acoustic, and mechanical metamaterials: an overview *Nanophotonics* **12** 659–86

[17] Meseguer F, Holgado M, Caballero D, Benaches N, Sanchez-Dehesa J, López C and Llinares J 1999 Rayleigh-wave attenuation by a semi-infinite two-dimensional elastic-band-gap crystal *Phys. Rev.* B **59** 12169

[18] Brûlé S, Javelaud E H, Enoch S and Guenneau S 2014 Experiments on seismic metamaterials: molding surface waves *Phys. Rev. Lett.* **112** 133901

[19] Wang J, Huang H W, Zhang B, Menq F-Y, Nakshatrala K B, Mo Y L and Stokoe K H 2022 Active isolation tests of metamaterial-based barriers and foundation *Eng. Struct.* **260** 114253

[20] Ramaswamy N, Joshi B, Wang J, Li X, Menq F Y, Shan X, Nakshatrala K B, Stokoe K H and Mo Y L 2023 Experimental study of passive seismic vibration isolation by trench-type periodic barrier *Eng. Struct.* **276** 115308

[21] Krushynska A O, Miniaci M, Bosia F and Pugno N M 2017 Coupling local resonance with Bragg band gaps in single-phase mechanical metamaterials *Extrem. Mech. Lett.* **12** 30–36

[22] Miniaci M, Krushynska A, Bosia F and Pugno N M 2016 *New J. Phys.* **18** 083041

[23] Achaoui Y, Antonakakis T, Brûlé S, Craster R V, Enoch S and Guenneau S 2017 Clamped seismic metamaterials: ultra-low frequency stop bands *New J. Phys.* **19** 063022

[24] Luo Y M, Huang T T, Zhang Y, Xu H H, Xie Y M and Ren X 2023 Novel meter-scale seismic metamaterial with low-frequency wide bandgap for Lamb waves *Eng. Struct.* **275** 115321

[25] Colombi A, Roux P, Guenneau S, Gueguen P and Craster R V 2016 Forests as a natural seismic metamaterial: rayleigh wave bandgaps induced by local resonances *Sci. Rep.* **6** 1–7

[26] Zeng Y, Xu Y, Deng K, Zeng Z, Yang H, Muzamil M and Du Q 2018 Low-frequency broadband seismic metamaterial using I-shaped pillars in a half-space *J. Appl. Phys.* **123** 214901

[27] Colquitt D J, Colombi A, Craster R V, Roux P and Guenneau S R L 2017 Seismic metasurfaces: sub-wavelength resonators and Rayleigh wave interaction *J. Mech. Phys. Solids* **99** 379–93

[28] Colombi A, Colquitt D, Roux P, Guenneau S and Craster R V 2016 A seismic metamaterial: the resonant metawedge *Sci. Rep.* **6** 27717

[29] Palermo A, Krödel S, Marzani A and Daraio C 2016 Engineered metabarrier as shield from seismic surface waves *Sci. Rep.* **6** 39356

[30] Palermo A, Vitali M and Marzani A 2018 Metabarriers with multi-mass locally resonating units for broad band Rayleigh waves attenuation *Soil Dyn. Earthq. Eng.* **113** 265–77

[31] Nistri F, Bosia F, Gliozzi A S, D'Alessandro L, Caverni S, Charkaluk P, Corigliano A, Miniaci M, Colombi A and Pugno N M 2024 Design and in field validation of a modular metamaterial for mitigation of railway induced vibrations *Soil Dyn. Earthq. Eng.* **180** 108594

[32] Russillo A F, Arena F and Failla G 2024 Water-tank metabarrier for seismic Rayleigh wave attenuation *Phil. Trans.* A **382** 20230363

[33] Xu Y, Pu X, Palermo A, Marzani A, Cai Y and Cao Z 2023 An analytical formulation to model geometric and resonant scattering of buried metabarriers for traffic-induced vibrations mitigation *Int. J. Solids Struct.* **270** 112237

[34] Krödel S, Thomé N and Daraio C 2015 Wide band-gap seismic metastructures *Extrem. Mech. Lett.* **4** 111–7

[35] Zeng Y, Xu Y, Deng K, Peng P, Yang H, Muzamil M and Du Q A 2019 A Broadband seismic metamaterial plate with simple structure and easy realization *J. Appl. Phys.* **125** 224901

[36] Zeng Y, Peng P, Du Q-J, Wang Y-S and Assouar B 2020 Subwavelength seismic metamaterial with an ultra-low frequency bandgap *J. Appl. Phys.* **128** 014901

[37] Miniaci M, Kherraz N, Croënne C, Mazzotti M, Morvaridi M, Gliozzi A S, Onorato M, Bosia F and Pugno N M 2021 Hierarchical large-scale elastic metamaterials for passive seismic wave mitigation *EPJ Appl. Metamater.* **8** 14

[38] Li T, Su Q and Kaewunruen S 2020 Seismic metamaterial barriers for ground vibration mitigation in railways considering the train-track-soil dynamic interactions *Constr. Build Mater.* **260** 119936

[39] Aguzzi G, Colombi A, Dertimanis V K and Chatzi E 2020 Metamaterials for groundborne vibration absorption in pillars *Proc. ISMA2020 Including USD2020* p 355

[40] Albino C, Godinho L, Amado-Mendes P, Alves-Costa P, Dias-da-costa D and Soares D Jr 2019 3D FEM analysis of the effect of buried phononic crystal barriers on vibration mitigation *Eng. Struct.* **196** 109340

[41] Ouakka S, Verlinden O and Kouroussis G 2022 Railway ground vibration and mitigation measures: benchmarking of best practices *Railway Eng. Sci.* **30** 1–22

[42] Zaccherini R, Palermo A, Marzani A, Colombi A, Dertimanis V K and Chatzi E N 2022 Geometric and material attenuation of surface acoustic modes in granular media *Geophys. J. Int.* **230** 288–97

[43] Colombi A, Zaccherini R, Aguzzi G, Palermo A and Chatzi E 2020 Mitigation of seismic waves: metabarriers and metafoundations bench tested *J. Sound Vib.* **485** 115537

[44] Lott M, Roux P, Garambois S, Guéguen P and Colombi A 2020 Evidence of metamaterial physics at the geophysics scale: the METAFORET experiment *Geophys. J. Int.* **220** 1330–9

[45] Miniaci M, Krushynska A, Gliozzi A S, Kherraz N, Bosia F and Pugno N M 2018 Design and fabrication of bioinspired hierarchical dissipative elastic metamaterials *Phys. Rev. Appl.* **10** 024012

[46] Coulier P, Cuéllar V, Degrande G and Lombaert G 2015 Experimental and numerical evaluation of the effectiveness of a stiff wave barrier in the soil *Soil Dyn. Earthq. Eng.* **77** 238–53

[47] Dijckmans A, Ekblad A, Smekal A, Degrande G and Lombaert G 2016 Efficacy of a sheet pile wall as a wave barrier for railway induced ground vibration *Soil Dyn. Earthq. Eng.* **84** 55–69

[48] Ghahari S F, Abazarsa F and Taciroglu E 2019 Identification of soil-structure systems *Seismic Structural Health Monitoring: From Theory to Successful Applications* ed M Limongelli and M Çelebi (Springer) pp 139–67

[49] Laude V 2020 *Phononic Crystals:. Artificial Crystals for Sonic, Acoustic, and Elastic Waves* (De Gruyter)

[50] Liu L and Hussein M I 2012 Wave motion in periodic flexural beams and characterization of the transition between Bragg scattering and local resonance *J. Appl. Mech.* **79** 011003

[51] Raghavan L and Phani A S 2013 Local resonance bandgaps in periodic media: theory and experiment *J. Acoust. Soc. Am.* **134** 1950–9

[52] Sharma B and Sun C T 2016 Local resonance and Bragg bandgaps in sandwich beams containing periodically inserted resonators *J. Sound Vib.* **364** 133–46

[53] Ravanbod M, Ebrahimi-Nejad S and Mollajafari M 2024 A thin-walled cavity structure with double-layer tapered scatterer locally resonant metamaterial plates for extreme low-frequency attenuation *Int. J. Solids Struct.* **293** 112742

[54] Ravanbod M and Ebrahimi-Nejad S 2023 Innovative lightweight re-entrant cross-like beam phononic crystal with perforated host for broadband vibration attenuation *Appl. Phys.* A **129** 102

[55] Krushynska A O, Gliozzi A S, Fina A, Krushinsky D, Battegazzore D, Badillo-Ávila M A, Acuautla M, Stassi S, Noè C and Pugno N M 2021 Dissipative dynamics of polymer phononic materials *Adv. Funct. Mater.* **31** 2103424

[56] Comina C, Foti S, Musso G and Romero E 2008 EIT oedometer: an advanced cell to monitor spatial and time variability in soil *Geotech. Test J. ASTM* **5** 404–12

[57] Lee J-S and Santamarina J C 2005 Bender elements: performance and signal interpretation *J. Geotech. Geoenviron. Eng.* **131** 1063–70

[58] Dal Poggetto V F, Pugno N M and de F. Arruda J R 2022 Bio-inspired periodic panels optimised for acoustic insulation *Phil. Trans.* A **380** 20210389